J. Dühn, C. Tessarek, M. Schowalter, T. Coenen, B. Gerken, K. Müller-Caspary, T. Mehrtens, M. Heilmann, S. Christiansen, A. Rosenauer, J. Gutowski, K. Sebald

Spatially resolved luminescence properties of non- and semi-polar InGaN quantum wells on GaN microrods

Spatially resolved luminescence properties of non- and semi-polar InGaN quantum wells on GaN microrods

J Dühn[1], C Tessarek[1,2], M Schowalter[1], T Coenen[3], B Gerken[1], K Müller-Caspari[1], T Mehrtens[1], M Heilmann[2], S Christiansen[2,4], A Rosenauer[1], J Gutowski[1] and K Sebald[1]

[1] Institute of Solid State Physics, University of Bremen, Otto-Hahn-Allee 1 28359 Bremen, Germany
[2] Max Planck Institute for the Science of Light, Günther-Scharowsky-Str. 1, D-91058 Erlangen, Germany
[3] DELMIC B.V., Kanaalweg 4, 2628 EB Delft, Netherlands
[4] Helmholtz-Zentrum Berlin für Materialien und Energie GmbH, Hahn–Meitner Platz 1, D-14109 Berlin, Germany

E-mail: duehn@ifp.uni-bremen.de

Received 21 March 2018, revised 8 July 2018
Accepted for publication 20 July 2018
Published 3 August 2018

Abstract

Spatially resolved emission properties of InGaN/GaN quantum wells on the facets of microrods are analyzed by means of photoluminescence and cathodoluminescence measurements. We observe strongly localized emissions of the non- and semi-polar InGaN quantum wells from the top part of the microrods, suggesting optical emitters of high efficiency. The quantum wells are characterized by transmission electron microscopy measurements with respect to their indium composition and thickness. Those wells oriented in non- and semi-polar directions possess high In concentrations as well as low internal polarization fields which makes these directions excellent candidates for InGaN quantum well emitters. These investigations show that the applied microrod growth concept is an effective method to realize high quality InGaN quantum wells on GaN facets oriented in non- and semi-polar directions which makes optoelectronic emitters in the green gap region feasible.

Keywords: InGaN, microrod, luminescence, non-polar, semi-polar, quantum well

(Some figures may appear in colour only in the online journal)

1. Introduction

InGaN-based quantum wells are of high importance for light sources due to the variability of the bandgap of the InGaN over the entire visible spectrum. Commonly used polar *c*-plane quantum wells (QWs) possess some disadvantages due to the presence of spontaneous and piezoelectric polarization which generate strong internal electric fields in these QW structures. The internal fields cause a spatial separation of electron and hole wave functions, resulting in a severe reduction of the carrier-recombination efficiency. This effect gets stronger with increasing indium concentration and well thickness which limits the emission wavelengths of InGaN to the blue spectral range. In order to overcome these limitations, many groups are working on the realization of emitters based on non- or semi-polar GaN heterostructures either without or reduced internal fields (reviews are given in [1, 2]). In addition to low internal fields, In incorporation is significantly higher in semi-polar directions [3]. Hence, the utilization of non- and semi-polar QWs provides the possibility of a wider spectral tuning range in comparison to polar InGaN-based emitters [4], thereby overcoming the problem of the green gap while retaining a high radiative recombination rate [2]. Additionally, a non-polar growth direction favors the incorporation of Mg which is of fundamental importance for electrically-pumped light emitters [5].

The growth of InGaN QW structures on off-axis crystallographic orientations requires GaN substrates which are cut on non- or semi-polar directions. These substrates are expensive, so in order to grow cost-efficient light emitters, cheaper

off-axis sapphire or silicon substrates have to be used. Due to the lattice mismatch, epitaxial layers grown on these substrates suffer from a very high density of defects, such as basal stacking faults and partial dislocations [2]. These defects introduce non-radiative recombination centers and thereby reduce the efficiency. Different groups have reported on improvement of the crystal quality of non-polar and semi-polar films grown on standard substrates by patterning the surface (e.g. [6, 7]). The utilization of micro-columns offers a method to reduce the density of defects and stacking faults, as, for example, reported for nanowires grown on patterned SiO_2 substrates [8]. Low defect densities were also observed for triangular core-shell nanowires with semi-polar InGaN/GaN QWs [9] as well as for InGaN/GaN multiple quantum well heterostructures grown on *m*- and *r*-planes of a single n-GaN nanowire [10]. In contrast to *a*-axis or *r*-axis oriented GaN-based nanowires, the growth of non-polar InGaN on *c*-axis oriented GaN is much easier. Hence, hexagonal core-shell GaN nanowires with non-polar InGaN/GaN multiple quantum wells (MQWs) have been extensively studied for technological applications [11–13]. Up to now, the prospects of non- and semi-polar orientated InGaN active layers have already been utilized for solar cells with improved carrier-collection efficiency [14], single nanowire lasers with significantly lower lasing thresholds due to high optical gain compared to nanowires with polar MQWs [15], and linearly polarized single photons from quantum dots contained in non-polar and semi-polar InGaN/GaN nanowires [16].

By using the facets of GaN microrods (MRs) as substrates for QW structures, one can obtain high crystalline qualities on standard substrates, with the additional benefit of achieving higher surface-to-volume ratios of the emitting layers in comparison to planar QW structures. These microrods can be grown using self-organizing processes [17] without the need for pre-patterned substrates. In addition, the microrod sidewalls define an optical resonator which supports whispering-gallery modes with high Q-factors [18] which allows for low-threshold lasing applications.

In this report, the spatial emission properties of core-shell MRs with non- and semi-polar QWs are comparatively analyzed by micro-photoluminescence (μ-PL) and cathodoluminescence (CL), giving insights into the spatial distributions with regard to the In content of the QWs as well as their radiation characteristics. These results are compared to TEM measurements of the InGaN QWs, from which the well thickness and In concentration can be obtained. Furthermore, an overview of the incorporation of indium for different crystallographic directions and polarities will be given.

2. Experimental

2.1. Growth of microrods (MOVPE)

The samples were grown on *c*-plane sapphire substrates by metal-organic vapor phase epitaxy (MOVPE; Aixtron 200RF). After thermal cleaning of the sapphire substrate in H_2 for 5 min and nitridation (NH_3 and H_2) for 10 min at 1200 °C (thermocouple temperature), GaN rods were deposited at 1150 °C starting with a high trimethylgallium (TMGa) precursor flow (40 sccm for 20 s) to initialize rod growth and changing to a low TMGa flow (10 sccm for 1040 s) to improve the optical properties [19]. Vertical growth of the rods was supported by a low V/III molar ratio of 25 and by excessive Si supply [20]. A thin layer of silicon nitride (SiN_x) is formed during growth on the sidewall facets of the MR which acts as an anti-surfactant layer and promotes the growth of microrods in *c*-direction [21]. The pressure in the chamber during growth was 100 mbar. After the growth of the rods, the sample was cooled down to room temperature (RT) and exposed to air. Before InGaN QW growth, the MR sample was annealed for 30 s and a GaN buffer layer was deposited for 60 s at 1130 °C in an H_2 atmosphere. The purpose was to reduce surface contamination and to completely cover the GaN rod with a new and clean GaN layer. The first InGaN QWs were grown for 20 s with a nominal In/(In + Ga) gas phase ratio of 0.6 followed by a GaN protection layer grown at 870 °C in an N_2 atmosphere. Afterwards, the atmosphere was changed to pure H_2 within 180 s. A GaN barrier layer was grown during a 150 s temperature ramp from 870 °C–1130 °C to end up with a high quality GaN layer needed for subsequent growth of the second and third InGaN QWs, respectively. After the third GaN barrier, a final GaN capping layer was grown for 150 s at 1130 °C.

2.2. Transmission electron microscopy

Specimens for transmission electron microscopy (TEM) were prepared using a FEI Nova focused ion beam (FIB) equipped with a Kleindieck MM3A-EM micro-manipulator. Free standing MRs were selected and covered with a layer of Pt using a gas injection system to protect two opposite $\{1\ \bar{1}\ 0\ 0\}$ side facets in the center of the MRs. These were then cut out with a part of the sapphire substrate, mounted to an omniprobe half-grid using the micro-manipulator and finally thinned to about 170 nm (value of the base; top thickness: 80 nm) to achieve transparency for electrons. The TEM specimens were then investigated in a FEI Titan 80–300ST equipped with a spherical aberration corrector of the objective lens, a Fischione (Model 3000) high-angle annular dark field (HAADF) detector, an EDAX detector for energy dispersive x-ray (EDX) spectroscopy, and a Gatan imaging filter (GIF). InGaN layer thicknesses and In concentrations were measured from high resolution HAADF-scanning TEM (STEM) images. For the latter, the raw HAADF images were normalized with respect to the incoming beam intensity, that was determined from a detector scan. The normalized intensities from regions with known composition (here GaN regions) are interpolated in regions with unknown intensity (here InGaN). Normalized intensities are directly comparable with frozen-phonon simulations (normalized intensity as a function of specimen thickness) and are used to derive the specimen thickness in the whole image. From the knowledge of specimen thickness and normalized intensity, the concentration in the InGaN layers can be determined from a comparison with a set of frozen phonon simulations (normalized intensity as a function of specimen thickness and in concentration).

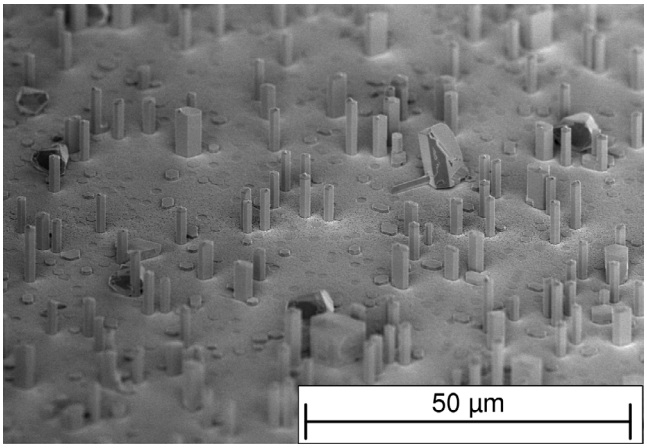

Figure 1. SEM image of as-grown microrods on the substrate, showing a random distribution and low uniformity.

For a more detailed explanation of the method see Rosenauer *et al* [22, 23]. Special care was taken to mitigate instrumental imperfections, as described by Krause *et al* [24]. Defects were characterized using conventional TEM applying weak beam dark field $\vec{g}/3\vec{g}$ imaging conditions.

2.3. Photo- and Cathodoluminescence

All luminescence measurements were conducted at room temperature. The CL was obtained by a SPARC cathodoluminescence imaging setup from DELMIC B.V. with a beam current of 120 pA and an acceleration voltage of 5 kV. This voltage corresponds to a penetration depth of about 105 nm for the electrons [25]. For the CL measurements, the sampling area on the sidewalls of the MR was 90×90 nm and for the measurement performed on the MR top 30×30 nm. For the μ-PL measurements, the 325 nm-line of a HeCd laser was used as an excitation source which has a penetration depth in bulk GaN of about 80 nm at RT [26]. In order to achieve a homogeneous PL excitation, the laser (28 mW output power) was widened to a diameter of about 25 μm which leads to an estimated excitation density of 9 kW cm^{-2}. The emission of the sample was imaged on a CCD (1340×400 pixel with a size of $13,5 \times 13,5$ μm) after passing the spectrometer.

3. Results and discussion

3.1. Structural characterization

Figure 1 shows an SEM overview of the as-grown structures. The density, height and diameter of the rods is ca. 10^6 cm^2, up to 7 μm and about 1.5 μm, respectively. The simple self-assembled and mask-free approach leads to a random rod distribution with a low uniformity. In order to enhance homogeniety of the samples a selective area growth [27] is recommended (not performed here). All rods consist of a Ga-polar core surrounded by a N-polar shell [28]. The polarity dependent termination of the surface leads to different stable facets [27], i.e. Ga-polar domains form top facets with a pyramidal shape while N-polar domains end up with flat top facets. Figure 2(a) shows an HAADF-STEM image of a microrod exhibiting a homogeneous width of 1.77 μm from base to top. A magnified HAADF-STEM image of the tip of the MR and the pyramid is depicted in figure 2(b) revealing that InGaN QWs can be found not only on the side facets of the column but on various other facets as well. Figure 2(c) shows a magnified image of the InGaN QWs deposited on the sidewalls of the microrod. The indium distribution in the upper part of the innermost and the two outermost QWs is homogeneous. In the lower part of the innermost InGaN QWs contrast fluctuations are observed, indicating a distorted incorporation of In. These disturbances correlate with the occurrence of dislocations (some indicated by arrows) that originate from the thin SiN_x layer present on the surface of the column prior to its overgrowth with the InGaN QWs. The SiN_x layer has been already observed and discussed in [18]. Figure 2(d) shows the In concentration map of the innermost InGaN QWs close to the edge (corresponding to a $(1\ 1\ 0\ 1)$ facet; #2 in figure 1(b)) of the InGaN QWs at the top of the MR. The In concentration therein was measured to be $(16 \pm 1)\%$, similar to that of the two outer QWs on this facet. In general, the In concentration in all three wells is alike for each facet with exception of the QWs distorted by the SiN_x. Figure 2(f) shows an In concentration map of the innermost InGaN QW in the transition region from a homogeneous to an inhomogeneous distribution of In. The concentration in In-rich regions can be as large as $(15 \pm 2)\%$, whereas $(7 \pm 1)\%$ were found in the homogeneous part of the layer. The latter concentration is in agreement with the composition of the two outermost InGaN QWs. The investigation of the two outermost QWs at various positions at the side-wall facet from the bottom to the top of the microrod reveals a homogeneous width and In concentration. In table 1, facet types, respective In concentrations, and thicknesses of the QWs are compared. Numbers in the first column correspond to the numbers in figure 2(b) and allow the assignment of quantities in table 1 to the respective facets. The $\{0\ 0\ 0\ 1\}$-, $\{1\ \bar{1}\ 0\ 0\}$- and $\{1\ \bar{1}\ 0\ \bar{1}\}$-planes are called *c*-plane, *m*-plane and *s*-plane, respectively. The innermost QW is significantly thicker than the two outer QWs for each facet. In figures 2(e)–(g), In concentration maps of the innermost and the outermost layer of facet #7 are depicted. For all QWs deposited on such high-index facets (#3, #7, #9), a step-like structure as well as a local enrichment of In at the edges of the steps (see figures 2(e)–(g)) can be found, as was already shown by Tessarek *et al* [18].

With the information on the properties of the QWs that were grown under the same growth conditions on different polarities, a comparison of the In corporation and growth rates of InGaN QWs can be made. Strict *c*-plane QWs were not formed in the N-polar material, however the high index $(\bar{1}\,1\,0\,\bar{2}\,4)$-plane is very similar, so this plane is used for comparison to the Ga-polar *c*-plane. In the *c*-plane, the In concentration is about the same for both polarities, however the thickness of the QWs in the Ga-polar direction is more than double that of N-polar QWs, indicating a faster growth rate of the Ga-polar material. The N-polar *s*-plane QW shows an 8-fold increased In concentration compared to the Ga-polar *s*-plane (#2 and #6 in table 1, respectively), as well as a thickness increased by a factor of 1.8 compared to the *m*-plane.

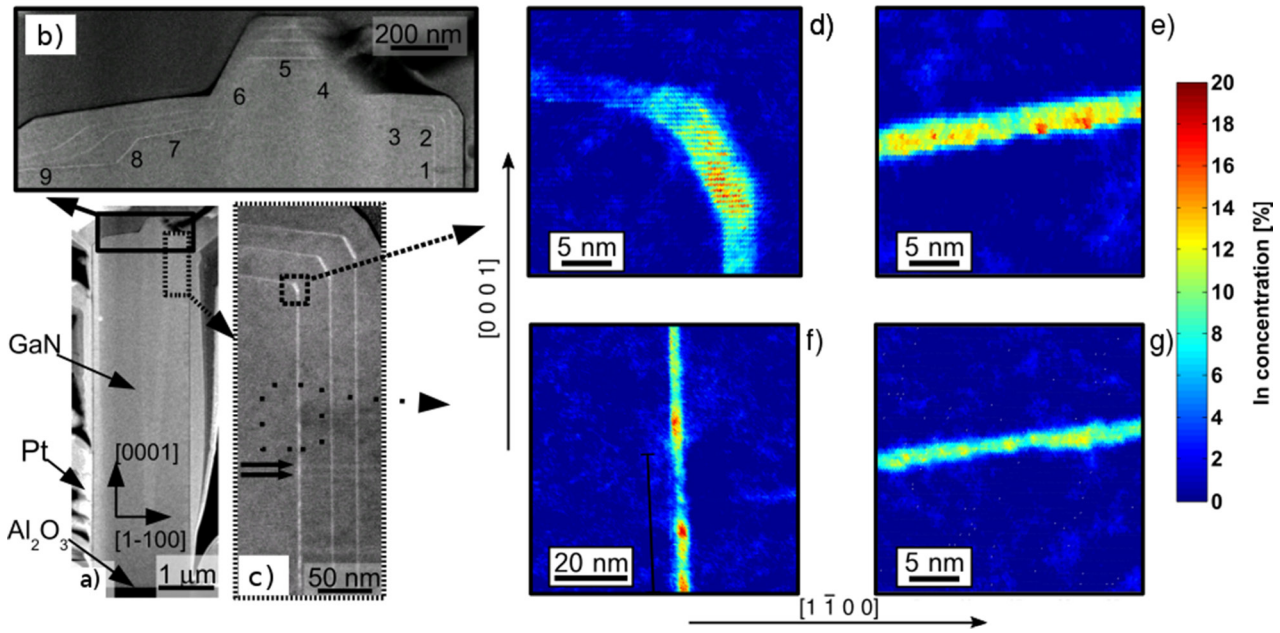

Figure 2. (a) HAADF-STEM image of a MR. (b) HAADF-STEM image of the tip of the MR exhibiting the nucleation of InGaN QWs on the various facets. (c) HAADF-STEM image at the top sidewall facets of the MR. (d) In concentration map of the innermost InGaN layer of facet #2 at the top of the MR. (e), (g) In concentration maps for the innermost and outermost InGaN QWs on a $(\bar{1}\ 1\ 0\ 1\bar{}2)$ facet. (f) In concentration map extracted from the HAADF data of the innermost InGaN QW in the transition region from a homogeneous to an inhomogeneous distribution of In.

Table 1. Overview of In concentrations, thicknesses and emission energies of various facets of the MR. Facet numbers correspond to the assignment in figure 2(b). The emission energies were determined by PL and CL measurements. The emission energies were calculated by the 1D-poisson solver aestimo [29], using the respective well thicknesses and In-concentrations.

				Thicknesses		Emission energy		
#	Facet plane	Name	Indium concentration (%)	Inner QW (nm)	Outer QWs (nm)	Observed (eV)	Calc. inner QW (eV)	Calc. outer QWs (eV)
1	$(1\ \bar{1}\ 0\ 0)$	*m*-plane	7 ± 1	3.7 ± 0.3	2.0 ± 0.3	3.16	3.224	3.295
2	$(1\ \bar{1}\ 0\ \bar{1})$	*s*-plane	16 ± 1	4.3 ± 0.3	3.6 ± 0.4	2.70	2.709	2.741
3	$(1\ \bar{1}\ 0\ 1\bar{}4)$	—	4 ± 2	3.7 ± 0.3	2.4 ± 0.3	—	3.288	3.353
4	$(1\ \bar{1}\ 0\ 1)$	*s*-plane	—	—	—	3.01	—	—
5	$(0\ 0\ 0\ 1)$	*c*-plane	9 ± 2	6.3 ± 0.3	5.1 ± 1	2.86	2.753	2.839
6	$(\bar{1}\ 1\ 0\ 1)$	*s*-plane	2 ± 1	—	2.0 ± 0.4	3.01	—	3.401
7	$(\bar{1}\ 1\ 0\ 1\bar{}2)$	—	11 ± 1	3.6 ± 0.3	2.0 ± 0.3	—	2.840	3.054
8	$(\bar{1}\ 1\ 0\ \bar{2})$	*r*-plane	11 ± 1	4.7 ± 0.3	3.7 ± 0.3	—	2.930	2.963
9	$(\bar{1}\ 1\ 0\ 2\bar{}4)$	—	9 ± 2	4.4 ± 0.3	2.1 ± 0.3	2.99	2.896	3.135

This demonstrates an efficient incorporation of In into N-polar *s*-plane QWs.

3.2. Analysis of sidewall emission

The spatially resolved emission of single MRs was measured by means of CL and μ-PL. In figure 3(a), spatially integrated PL and CL overview spectra of two different MRs are shown. The small contribution at 3.39 eV can be attributed to the GaN-related near-band-gap emission (NBE). According to TEM measurements (figure 2), no pure *c*-plane InGaN QWs were formed, however the high-indexed facets (positions #7 and #9 in figure 2(b)) have an inclination close to the *c*-plane. Their average In content and thickness is about 10% and 2 nm, respectively, which yields an emission energy of 3.1 eV. The QW on positions #2, #4, #6 and #8 have a semi-polar orientation and the polarization field strengths in these wells are expected to reach just 20% of those in polar QWs for comparable thickness and In concentration [3]. The linewidth deduced from the spectrum is in the order of 230 meV (full width half maximum) for the semi- and non-polar QWs. This rather large value is only slightly higher compared to

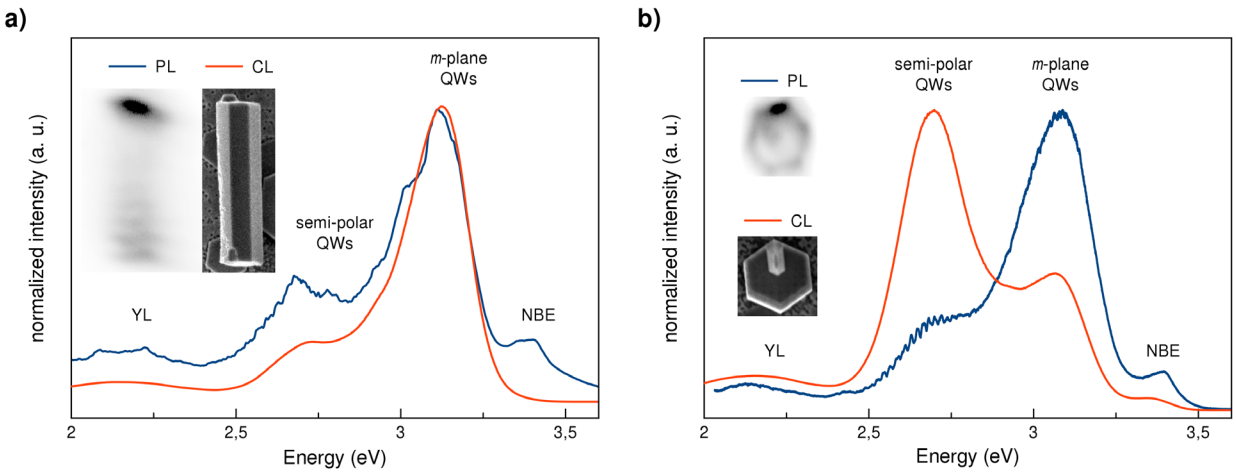

Figure 3. Spatially integrated photo- and cathodoluminescence of a MR detached from substrate (a) and of the top facet of a free standing MR (b). The measurements were performed at room temperature on different MRs. The emission bands from the GaN (NBE, YL), from the non-polar $\{1\ \bar{1}\ 0\ 0\}$ and the semi-polar $\{1\ \bar{1}\ 0\ \bar{1}\}$ QWs can be identified. The insets display the PL (left, dark areas correspond to highest emission intensities) and SEM (right) images of the investigated MRs.

linewidths reported for CL and PL of SQW MR (190 meV [30], 140 meV [31]) and single MRs with MQW have values from 100 to 175 meV [11] increasing with the incorporated In content. The intensity of the PL spectrum shows in comparison to the CL spectrum a small periodic modulation of the intensity in the region of the interface QW emission. By taking the Fabry–Perot interference into account, the distance of the intensity maxima correspond to the length of the MR. This periodicity can be identified as well at the bottom part of the emission image of the MR, as it was mapped on the entrance slit of the spectrometer (left inset, black corresponds to the brightest intensity). At about 2.2 eV, the defect-related yellow luminescence (YL) of GaN can be identified. In order to obtain spatially resolved μ-PL, the image of the MR (see inset of figure 3(a), black corresponds to the brightest intensity) was focused on the entrance slit of the spectrometer. At the energy of the assigned emission bands, spatially resolved spectra were recorded as an image on the CCD, as shown in figure 4. The vertical axis corresponds to the c-axis of the MR while the horizontal axis shows the emission energy. The intensity is given as a color-coded map. The spatially resolved μ-PL is compared to spatially resolved CL measurements, conducted on different MRs. The spatially (vertical axes) and spectrally (horizontal axes) resolved emission of the assigned bands is compared as obtained under μ-PL and CL conditions in the left and middle column of figure 4(a), respectively. A 2D CL map at the respective mean energy of the row is displayed in the right column. The NBE of the GaN in μ-PL shows faint emission over the entire microrod length with its maximum localized at the top and some contributions from the lower part of the MR. The first 600 nm of the MR show a diminished intensity of NBE, presumably due to high defect densities induced by the lattice mismatch between the sapphire substrate and the GaN. The non-polar QW emission (figure 4(a)) is predominantly centered at the top part of the MR in PL and CL. This strong localization of emission is prominent in almost all spectral regions and corresponds to the SiN_x-free part of the MR, where the TEM images have shown an absence of extended defects. The SiN_x layer acts as an anti-surfactant which promotes the growth of MRs but also yields poor crystalline qualities for structures grown directly on it. A small contribution from the bottom part of the MR which originates from small spots at the surface related to structural defects which can be seen in CL (middle and right column of row 2 in figure 4(a)). The emission from the semi-polar QWs, displayed in the last row, is slightly less intense than the emission from the non-polar QWs, and even more strongly localized at the top, as one would expect from the TEM results (figure 2(d)). In PL, there is a faint intensity along the MR with a periodic intensity modulation at the lower part suggesting the formation of an optical resonator, as already observed in the PL emission image (inset of figure 3(b)).

3.3. Analysis of top facet emission

In figure 3(b), spatially integrated PL and CL overview spectra from the tops of two different MRs are shown. Again, the emission band of the GaN-related NBE and YL, the contribution from the m-plane InGaN QWs, and the emission of the s-plane QWs can be identified. The intensity contributions from the free-standing MR are similar to that of detached MR in PL. However, in CL the emission from the s-plane QWs is enhanced with respect to m-plane QWs for free-standing MRs. This is due to the fact that the maximum detection angle in PL is limited by the numerical aperture of the microscope objective (NA = 0.5) to about 30° while for CL measurements the MR is surrounded by a parabolic mirror detecting emission angles up to 88° with respect to the surface. Hence, the emission of semi-polar QWs is detected much more efficiently in CL than in μ-PL, since the s-plane is inclined about 60° with respect to the growth axis (see figure 2(d)).

In order to obtain the spatially resolved μ-PL of the top facet, the emission image of the MR, shown in the inset of figure 3(b) (black corresponds again to the brightest intensity),

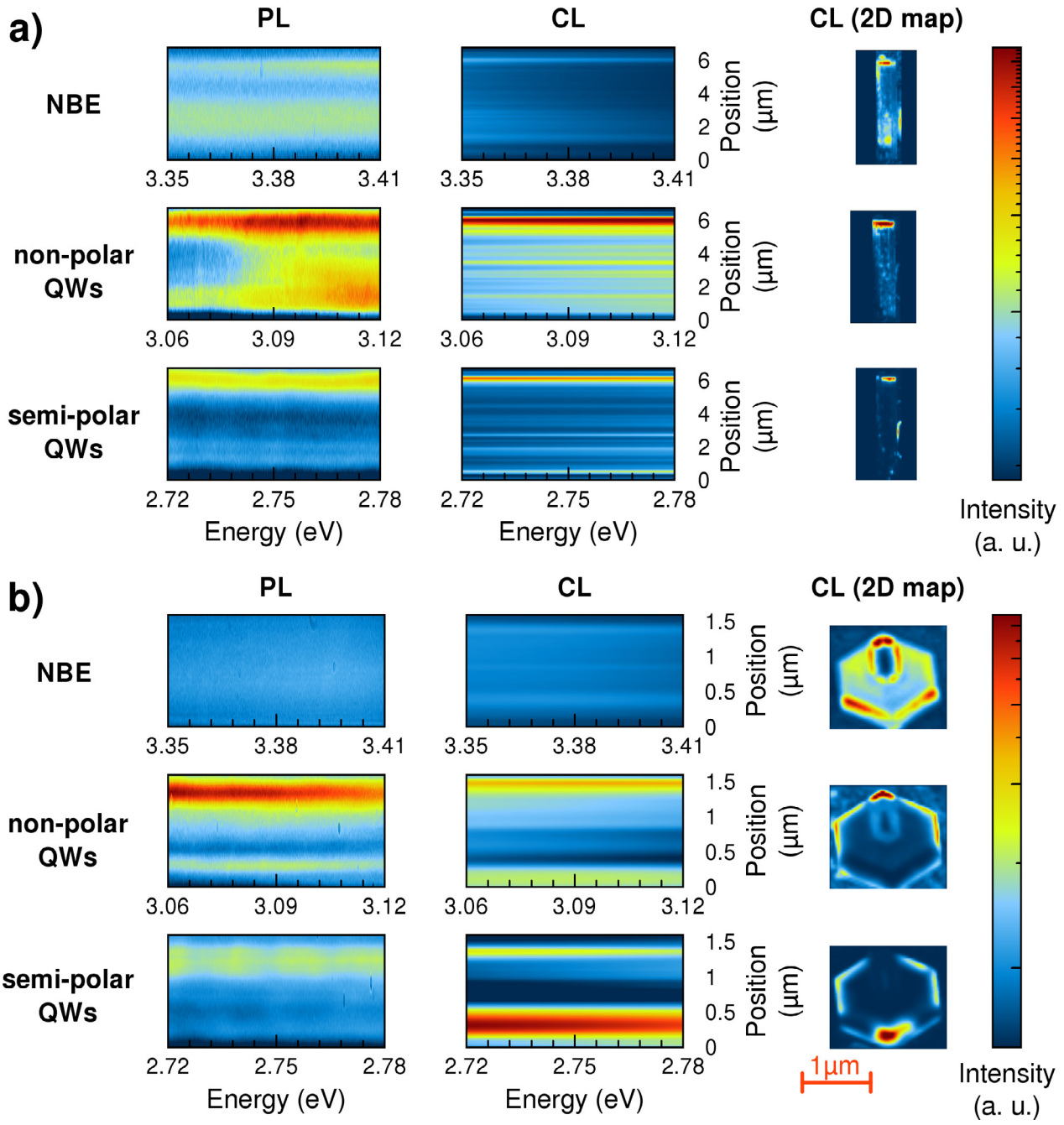

Figure 4. (a) Spatially resolved PL and CL of a MR along the *c*-axis and (b) of the top facet. On the left side, CCD images of the PL in the given energy region are shown. The middle image column shows the spatially resolved CL excitation in the same energy range as the PL on the left column. The right image column shows CL maps along the rod (upper three pictures in (a)) and of the top facet (lower three pictures, (b)) integrated over the three different energy ranges defined in the left-hand figures, respectively. The intensities are color-coded on a logarithmic scale and show that the emission from the non- and semi-polar InGaN QWs is strongly localized at the top of the MR. In CL, the intensities were normalized for each emission energy.

was focused on the entrance slit of the spectrometer. Although the excitation laser spot was expanded, in order to achieve an almost homogeneous excitation of the entire MR surface, the emission image shows a black spot indicating an area of localized, high emission intensity. In figure 4(b), the GaN-related NBE centered at 3.39 eV can be seen as a faint emission with no particular localization, as expected for the uniformly distributed GaN core and barrier material. The emission from the N-polar *s*-plane QWs shows the highest intensity, centered at about 2.75 eV, with a strong localization at the edges of the hexagon (second row of figure 4(b)). These findings are in agreement with the observed increased incorporation of indium at the edges and at the interfaces of the MR as already discussed for the TEM results. In addition, the PL emission band of the semi-polar QWs at 2.75 eV exhibits a periodic modulation of the intensity distribution (left-hand figure in third row of figure 4(b)) as already observed in the overview spectrum (figure 3(b)). The modulation corresponds to

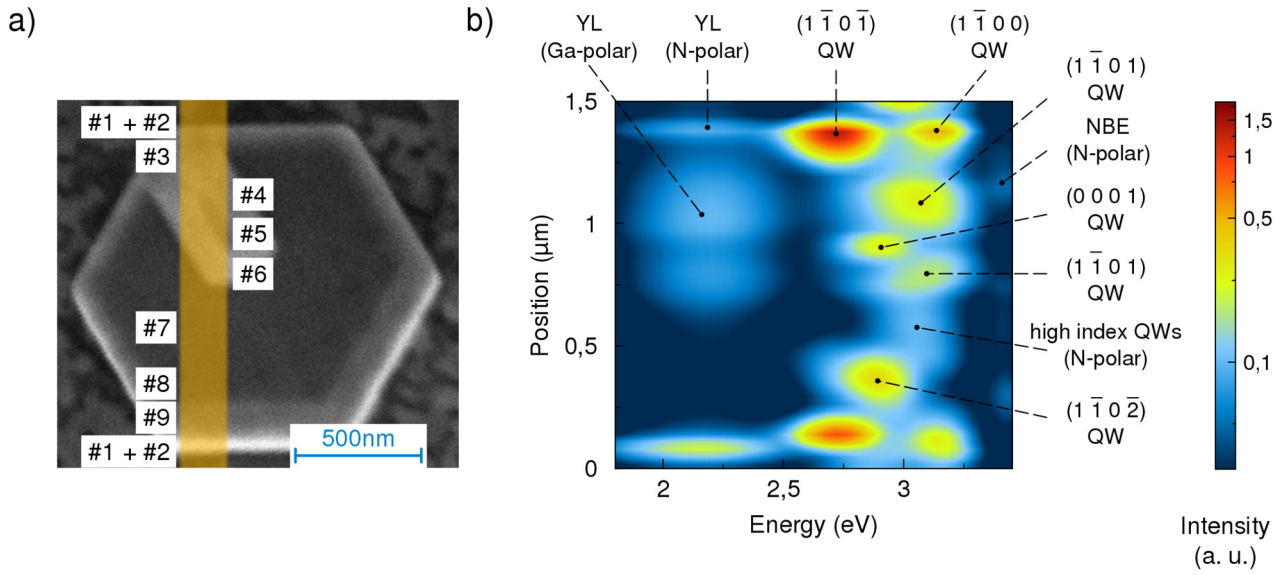

Figure 5. (a) SEM image of the top of the MR with the numbering of the QWs as assigned in figure 2. (b) Integrated CL emission when excited along the path depicted as orange line in (a). The intensity is color-coded on a logarithmic scale. The width of the orange line (180 nm) corresponds to the area of the integrated CL.

whispering gallery modes and was already reported for similar MR structures [18]. The combination of spatially resolved PL and CL measurements on the top of these MRs shows the strong localization in the non- and semi-polar InGaN QW emission of the MR.

A more detailed analysis of the top facet can be seen in figure 5. In figure 5(a), the excitation path over the top facet is represented by the orange line, where a spatially resolved CL measurement was conducted and is shown in figure 5(b). The emission from the N-polar QWs dominates the spectrum and is concentrated at the borders of the microrod, where the *s*- and *m*-planes are located. Small luminescence contributions from the N-polar high-index-plane QWs and the near-bandgap emission can be observed whereas the YL band is almost absent. For these polar QWs, the piezoelectric field causes a strong reduction of the wave function overlap, resulting in a reduced recombination probability in comparison to non-polar QWs. Combining the results observed in figures 2, 4 and 5, it is evident that the outer rim of the Ga-polar tip predominantly emits in the spectral region of the GaN-related near-band emission and the emission of the m-plane InGaN. A moderate intensity can be found at the local position labeled in figure 2 with #1, #2 and #3, which can be found at the left/upper and right/lower MR edge relative to the Ga-polar tip as well. The semi-polar InGaN-emission seems to be localized at the opposite edge of the GaN-polar tip (figure 4) with a small contribution at the left/upper and right/lower MR edge relative to the Ga-polar tip (figure 5) and the position coincides with the labels #9, #8 and #7 in figure 2. These findings are in agreement with the observed increased In incorporation at the facet #7 shown for the TEM results in figures 2(e) and (f). The emission from the Ga-polar *c*- and *s*-plane QWs from the pyramid can be identified in the middle of the MR. Concerning the GaN barriers, the presence of YL and absence of NBE emission is noteworthy which is in accordance with the features of non- and semi-polar QW emission. This is a hint towards the existence of point defects in these directions. It is rather unlikely that carbon stemming from the precursors is introduced and causes the YL emission since the incorporation of carbon should be highest in *c*-plane [32] which is almost free of YL. Ga vacancies could be a more reasonable source of YL emission since they form more rapidly on the N-polar *s*-plane growth direction than in the *c*-plane [33] for N-rich environments. Indium supplied during growth should lead to a serious reduction of the density of Ga vacancies [34]. Indium is efficiently incorporated especially in the N-polar s-plane QWs which explains their high In content.

4. Conclusion

The structural and optical properties of InGaN QWs on self-catalyzed core-shell InGaN/GaN microrods grown by MOVPE were analyzed by PL, CL and TEM measurements. The latter revealed the top part of the MRs to be of high crystalline quality. Further, a multitude of differently oriented QWs were formed on the various facets. A detailed analysis regarding the thicknesses and indium contents of these QWs was conducted, allowing for a comparison of growth properties with respect to different crystallographic orientations as well as polarities. The combination of spatially resolved PL and CL allowed for a deep insight into the localization distribution of the emission contributions. Areas of high luminescence intensity originate predominantly from QWs grown on the top facets of the microrods, were observed from non- and semi-polar InGaN QWs. The small internal fields and the possibility of a high In incorporation is favorable for optoelectronic applications in the green gap region which may be realized by optimizing the contribution of this emitter type and by increasing the MR density before developing LEDs based on the p-GaN overgrowth technique [35].

Acknowledgments

J D and K S thank the Central Research Development Fund of the University of Bremen for financial funding. Funding has also been granted by the DFG (German Research Society) through the Research Unit FOR 1616 'Dynamics and Interactions of Semiconductor Nanowires for Optoelectronics' and the DFG Collaborative Research Center SFB 951 'HIOS: Hybrid Inorganic/Organic Systems for Opto-Electronics' (project number SFB 951).

ORCID iDs

J Dühn https://orcid.org/0000-0003-4129-3826
C Tessarek https://orcid.org/0000-0003-4126-3694
M Heilmann https://orcid.org/0000-0002-5485-1244

References

[1] Zhao Y, Farrell R M, Wu Y R and Speck J S 2014 *Japan. J. Appl. Phys.* **53** 100206
[2] Wang T 2016 *Semicond. Sci. Technol.* **31** 093003
[3] Wernicke T, Schade L, Netzel C, Rass J, Hoffmann V, Ploch S, Knauer A, Weyers M, Schwarz U and Kneissl M 2012 *Semicond. Sci. Technol.* **27** 024014
[4] Bai J, Xu B, Guzman F G, Xing K, Gong Y, Hou Y and Wang T 2015 *Appl. Phys. Lett.* **107** 261103
[5] McLaurin M, Mates T E and Speck J S 2005 *Appl. Phys. Lett.* **86** 262104
[6] Reuters B, Strate J, Wille A, Marx M, Lükens G, Heuken L, Heuken M, Kalisch H and Vescan A 2015 *J. Phys. D: Appl. Phys.* **48** 485103
[7] Rishinaramangalam A K, Nami M, Fairchild M N, Shima D M, Balakrishnan G, Brueck S R J and Feezell D F 2016 *Appl. Phys. Express* **9** 059201
[8] Bae S Y *et al* 2017 *Sci. Rep.* **7** 45345
[9] Qian F, Li Y, Gradečak S, Park H G, Dong Y, Ding Y, Wang Z L and Lieber C M 2008 *Nat. Mater.* **7** 701–6
[10] Ra Y H, Navamathavan R, Kang S and Lee C R 2014 *J. Mater. Chem.* C **2** 2692
[11] Koester R *et al* 2011 *Nano Lett.* **11** 4839–45
[12] Yeh T W, Lin Y T, Stewart L S, Dapkus P D, Sarkissian R, O'Brien J D, Ahn B and Nutt S R 2012 *Nano Lett.* **12** 3257–62
[13] Ra Y H, Navamathavan R, Yoo H I and Lee C R 2014 *Nano Lett.* **14** 1537–45
[14] Huang X, Fu H, Chen H, Zhang X, Lu Z, Montes J, Iza M, DenBaars S P, Nakamura S and Zhao Y 2017 *Appl. Phys. Lett.* **110** 161105
[15] Li C *et al* 2017 *Nano Lett.* **17** 1049–55
[16] Gačević Z *et al* 2017 *ACS Photon.* **4** 657–64
[17] Tessarek C, Bashouti M, Heilmann M, Dieker C, Knoke I, Spiecker E and Christiansen S 2013 *J. Appl. Phys.* **114** 144304
[18] Tessarek C, Rechberger S, Dieker C, Heilmann M, Spiecker E and Christiansen S 2017 *Nanotechnology* **28** 485601
[19] Tessarek C *et al* 2014 *ACS Photon.* **1** 990–7
[20] Koester R, Hwang J S, Durand C, Le Si Dang D and Eymery J 2010 *Nanotechnology* **21** 015602
[21] Tessarek C, Heilmann M, Butzen E, Haab A, Hardtdegen H, Dieker C, Spiecker E and Christiansen S 2014 *Cryst. Growth Des.* **14** 1486–92
[22] Rosenauer A, Gries K, Müller K, Pretorius A, Schowalter M, Avramescu A, Engl K and Lutgen S 2009 *Ultramicroscopy* **109** 1171–82
[23] Rosenauer A *et al* 2011 *Ultramicroscopy* **111** 1316–27
[24] Krause F F, Schowalter M, Grieb T, Müller-Caspary K, Mehrtens T and Rosenauer A 2016 *Ultramicroscopy* **161** 146–60
[25] Robins L H, Bertness K A, Barker J M, Sanford N A and Schlager J B 2007 *J. Appl. Phys.* **101** 113505
[26] Muth J F, Lee J H, Shmagin I K, Kolbas R M, Casey H C, Keller B P, Mishra U K and DenBaars S P 1997 *Appl. Phys. Lett.* **71** 2572
[27] Li S F, Fuendling S, Wang X, Merzsch S, Al-Suleiman M A M, Wei J D, Wehmann H H, Waag A, Bergbauer W and Strassburg M 2011 *Cryst. Growth Des.* **11** 1573–7
[28] Tessarek C, Figge S, Gust A, Heilmann M, Dieker C, Spiecker E and Christiansen S 2014 *J. Phys. D: Appl. Phys.* **47** 394008
[29] Steed R, Hebal H and Lisesivdin S B 2017 sblisesivdin/aestimo: version v.1.2 *(version v.1.2.0) Zenodo* (http://doi.org/10.5281/zenodo.1042657)
[30] Müller M *et al* 2016 *Nano Lett.* **16** 5340–6
[31] Mounir C, Schimpke T, Rossbach G, Avramescu A, Strassburg M and Schwarz U T 2016 *J. Appl. Phys.* **120** 155702
[32] Cruz S C, Keller S, Mates T E, Mishra U K and DenBaars S P 2009 *J. Cryst. Growth* **311** 3817–23
[33] Akiyama T, Ammi D, Nakamura K and Ito T 2009 *Japan. J. Appl. Phys.* **48** 100201
[34] Chung H M, Chuang W C, Pan Y C, Tsai C C, Lee M C, Chen W H, Chen W K, Chiang C I, Lin C H and Chang H 2000 *Appl. Phys. Lett.* **76** 897–9
[35] Jung B O, Bae S Y, Lee S, Kim S Y, Lee J Y, Honda Y and Amano H 2016 *Nanoscale Res. Lett.* **11** 215